Evidence for auroral influence on Jupiter's stratospheric composition revealed by ALMA

Thibault Cavalié (thibault.cavalie@u-bordeaux.fr)
Laboratoire d'Astrophysique de Bordeaux https://orcid.org/0000-0002-0649-1192

Ladislav Rezac
Max Planck Institute for Solar System Research https://orcid.org/0000-0003-3299-425X

Raphael Moreno
Paris Observatory https://orcid.org/0000-0002-9171-2702

Emmanuel Lellouch
Observatoire de Paris https://orcid.org/0000-0001-7168-1577

Thierry Fouchet
Observatoire de Paris https://orcid.org/0000-0001-9040-8285

Bilal Benmahi
Université de Bordeaux

Thomas Greathouse
Southwest Research Institute

James Sinclair
Jet Propulsion Laboratory/California Institute of Technology https://orcid.org/0000-0001-5374-4028

Vincent Hue
Southwest Research Institute

Paul Hartogh
Max-Planck-Institut für Sonnensystemforschung (MPS)

Michel Dobrijevic
Laboratoire d'Astrophysique de Bordeaux

Nathalie Carrasco
Versailles Saint-Quentin-en-Yvelines University https://orcid.org/0000-0002-0596-6336

Zoé Perrin
LATMOS

Article

Keywords:

Posted Date: December 1st, 2022

DOI: https://doi.org/10.21203/rs.3.rs-2165172/v1

Additional Declarations: There is **NO** Competing Interest.

Version of Record: A version of this preprint was published at Nature Astronomy on July 6th, 2023. See the published version at https://doi.org/10.1038/s41550-023-02016-7.

Evidence for auroral influence on Jupiter's stratospheric composition revealed by ALMA

Authors: T. Cavalié[1, 2]*, L. Rezac[3], R. Moreno[2], E. Lellouch[2], T. Fouchet[2], B. Benmahi[1], T. K. Greathouse[4], J. A. Sinclair[5], V. Hue[4], P. Hartogh[3], M. Dobrijevic[1], N. Carrasco[6], Z. Perrin[6]

Affiliations:

[1]Univ. Bordeaux, CNRS, LAB, UMR 5804, F-33600 Pessac, France (ORCID: 0000-0002-0649-1192)

[2]LESIA, Observatoire de Paris, PSL Research University, CNRS, Sorbonne Universités, UPMC Univ. Paris 06, Univ. Paris Diderot, Sorbonne Paris Cité, Meudon, France

[3]Max-Planck-Institut für Sonnensystemforschung, 37077 Göttingen, Germany

[4]Southwest Research Institute, San Antonio, TX 78228, United States

[5]Jet Propulsion Laboratory, California Institute of Technology, 4800 Oak Grove Drive, Pasadena, CA 91109, USA

[6]LATMOS, CNRS, UVSQ Université Paris-Saclay, Sorbonne Université ; 11 boulevard d'Alembert, 78280 Guyancourt, France

*Corresponding author. Email: thibault.cavalie@u-bordeaux.fr

Abstract: The localized delivery of new long-lived species to Jupiter's stratosphere by comet Shoemaker-Levy 9 in 1994 opened a window to constrain jovian chemistry and dynamics by monitoring the evolution of their vertical and horizontal distributions. ALMA observations of HCN and CO in March 2017 show that CO was meridionally uniform and restricted to pressures lower than 3±1 mbar. HCN shared a similar vertical distribution in the low-to-mid latitudes, but was surprisingly depleted at pressures higher than $0.04^{+0.07}_{-0.03}$ mbar in the polar regions. We propose that heterogeneous chemistry bonds HCN on large aurora-produced aerosols at these pressures in the jovian polar regions causing the observed depletion. We also propose that a relatively small fraction of CO causes enhanced production of CO_2 inside the aurora to explain the long-term decrease of the CO column density and the CO_2 peak observed only at southern polar latitudes in 2000.

Jupiter is an archetype for gas giants (in the solar system and in extrasolar systems). Like the other giants in the Solar System, it is a fast rotator (9.9-hr period). The sheer size and angular speed induce a very complex atmospheric structure, circulation and meteorological system such that the mechanisms at work in Jupiter's atmosphere are still poorly understood. General Circulation Models (GCM) for giant planets are in development (*e.g., 1*) to understand these processes.

Mainly composed of hydrogen and helium, giant planets also contain 0.2-4% methane. Its photolysis at high altitude initiates the production of more complex hydrocarbons (*2*). Giant planets also capture external material, in the form of infalling comets, interplanetary dust, or gas and grains from their ring and satellite systems (*3*), contributing to the chemical complexification of their atmospheres. While 1D photochemical models generally succeed in explaining the disk-averaged abundances of these species (*2*), no model has yet managed to understand the meridional distributions and the temporal evolution of their hydrocarbons and other trace species (e.g., *4, 5*).

A rare event at Jupiter can help us better constrain both chemistry and dynamics in Jupiter's atmosphere. July 1994 saw the first extraterrestrial collision in the Solar System witnessed from Earth with multi-spectral observations. The 21 fragments of comet Shoemaker Levy 9 (SL9) spectacularly impacted Jupiter in its southern hemisphere near 44°S, increased its temperature

locally (*6, 7*) and left the planet with visible dark scars for weeks (e.g., *8*). Even more significant on the long term, the SL9 impacts produced a series of species previously undetected in the stratosphere, like CO, HCN, CS, H_2O, and CO_2 (*9-11*), probably from shock chemistry during the impacts (*12*), except CO_2 which probably formed subsequently from atmospheric photochemistry (*13*). These species were deposited at ~0.1 mbar during the splashback of the impact plumes (*14, 15*), and subsequently started to spread in Jupiter's stratosphere. While they contaminated all longitudes at the impact site latitude within approximately one year (*16*), the meridional and vertical diffusion occurred on longer timescales. *(15)* predicted that meridional mixing would require more than a decade to see abundances uniformly mixed. This was confirmed by observations of HCN and CO_2 in 1995 and 2000 by *(17)* and *(18)* and the long-term monitoring of the H_2O vertical distribution by *(19-21)*. Given that CO, HCN, CS and H_2O have sufficiently long chemical lifetimes (>10 years), their deposition by SL9 in 1994 offers us a unique opportunity to study the temporal evolution of their distributions over several years and now decades. This is a powerful tool to better understand the chemistry and dynamics of Jupiter's stratosphere.

CO, HCN, and CS, have been monitored ever since the SL9 impacts. *(15)* have mapped their distributions until 1998 with a moderate spatial resolution of 1/3–1/4 of the planet diameter. Further monitoring over the following decade consistently showed a slow decrease of their disk-averaged masses, reaching a factor of 5 to 15 decay between 1998 and 2006. Despite the slow decrease of their abundances, CO, HCN, and CS, are stable enough that they can be used as dynamical tracers in the Jovian atmosphere, using their vertical and latitudinal distributions. Based on observations over 1994-1997 with the IRAM-30m and the IRTF, *(15)* and *(17)* obtained the first estimates on latitudinal eddy mixing. *(17)* revealed that, in addition to a large S-N hemispheric asymmetry, HCN showed an abrupt decrease southward of 45°S, that was interpreted as a "dynamical barrier" isolating the southern polar region from other latitudes.

Most remarkably, CO_2, observed simultaneously with HCN by *Cassini*, revealed a strikingly different distribution from HCN, peaking at the South Pole instead (*18*). The difference is difficult to understand as CO_2 is thought to be a daughter molecule of CO (from $CO+OH \rightarrow CO_2 + H$, where OH is produced from H_2O) (*13*), which was produced by the SL9 impacts, similar to HCN. *(18)* explored models in which the CO_2 polar excess was associated with the conversion of precipitating oxygen-bearing material to CO_2, but did not find this to be a promising scenario. *(18)* also investigated various horizontal transport models combining latitudinal advection and strongly latitude-dependent eddy mixing and tentatively concluded that the HCN and CO_2 were affected by meridional transport in opposite directions (equatorward and poleward, respectively), implying that the two species resided at different atmospheric levels. The conclusions were however strongly hampered by the lack of information on the behavior of CO.

We mapped the HCN (4-3) and CO (3-2) spectral emissions in Jupiter's stratosphere with the Atacama Large Millimeter/submillimeter Array (ALMA) on March 22nd, 2017, to retrieve the spatial distribution of these species and better understand their temporal evolution. More details on the observations can be found in Section 1 of the Supplementary Material. We used the combination of temperature maps obtained nearly simultaneously to our observations, a forward radiative transfer modeling and a retrieval algorithm, all detailed in Section 2 of the Supplementary Material, to retrieve the vertical profiles of HCN and CO as a function of latitude from spectra observed at the limb of Jupiter.

The spatial distribution of CO and HCN

The whole set of retrieved CO vertical profiles is shown in Figure 1 and we took these profiles to compute the column density as a function of latitude. The meridional distribution of CO is displayed in Figure 2. It essentially shows that CO was rather uniformly mixed as a function of

latitude in Jupiter's stratosphere as of March 2017. We can then put a lower limit on meridional mixing. For CO to populate all latitudes starting from the impact latitude in maximum $\Delta t = 22.5$ years, it requires $K_{yy} \sim \frac{L^2}{\Delta t} \geq 3.7 \times 10^{11}$ cm^2.s^{-1} around mbar pressures, with L the distance from 44°S to the north pole. This is consistent with the values derived by *(13, 15, 18)*. With the 3-parameter fit profile, we find a CO mole fraction of 41±12 ppb (1-σ uncertainty) above an average cut-off pressure of 3±1 mbar. The resulting meridionally uniform CO column density is 1.65±0.50 × 10^{15} cm^{-2}. The total mass of SL9-derived CO is then 4.87±0.23 × 10^{13} g, which corresponds to a loss factor of 10±3 since 1995-1998 (*15*).

The distribution of HCN shows significant variability as seen in Figure 3. And surprisingly, this variability is not simply a function of latitude as demonstrated by the column density meridional profiles on each limb (Figure 2). It is rather constant from ~55°S to ~40°N with a value of 18.1±6.5 × 10^{12} cm^{-2}. In this region, we find an HCN mole fraction of 0.9±0.5 ppb (1-σ uncertainty) above an average cut-off pressure of 2^{+2}_{-1} mbar. The variability seen in the HCN column density in this latitudinal range is caused by the continuum subtraction performed at the data reduction stage. It is done using a uniform disk model which does not perfectly fit the zone/belt structure of Jupiter's continuum. The line-to-continuum ratio (and thus the retrieved value of the HCN mole fraction at high altitude) is consequently altered. We find a similar structure in the variability of the CO column density profile in this latitudinal range and it is thus also not a real feature. At latitudes southward of ~70°S, northward of 50°N on the western limb, and northward of 65°N on the eastern limb, the HCN column density drops by a factor of 25–100 with respect to the low-to-mid latitudes. This drop is caused by a depletion of the HCN vertical profile at millibar pressures. Indeed, the vertical distributions retrieved in these regions shows a cut-off pressure at $0.04^{+0.07}_{-0.03}$ mbar. We will come back to the local increase in this region between 75°S and 85°S on the eastern limb later. Integrating the HCN column density meridional profile, we find a total mass of 4.0±0.1 × 10^{11} g. This corresponds to a loss factor of 60±35 when compared with the 1995-1998 period (Moreno et al. 2003), or 150±40 when compared with the value derived in 2000 from the Cassini flyby data[1] (*18*).

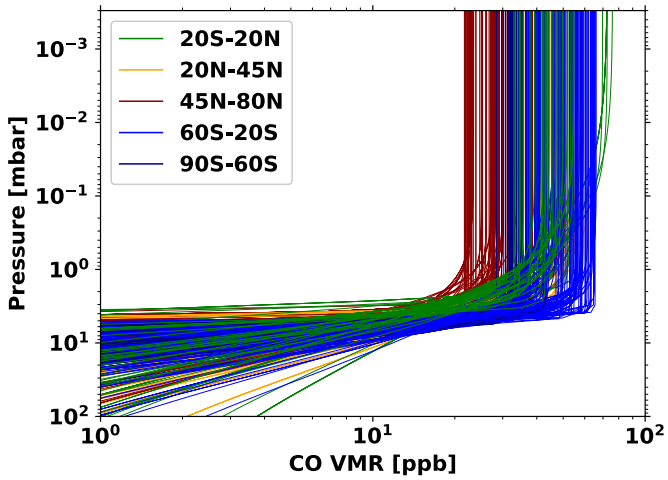

Figure 1 CO vertical profiles in Jupiter's stratosphere, as retrieved from the ALMA observations of March 2017. They are plotted by latitude bins.

[1] (*18*) investigated the HCN mass increase from the secondary production of HCN from NH_3 following the comet impacts.

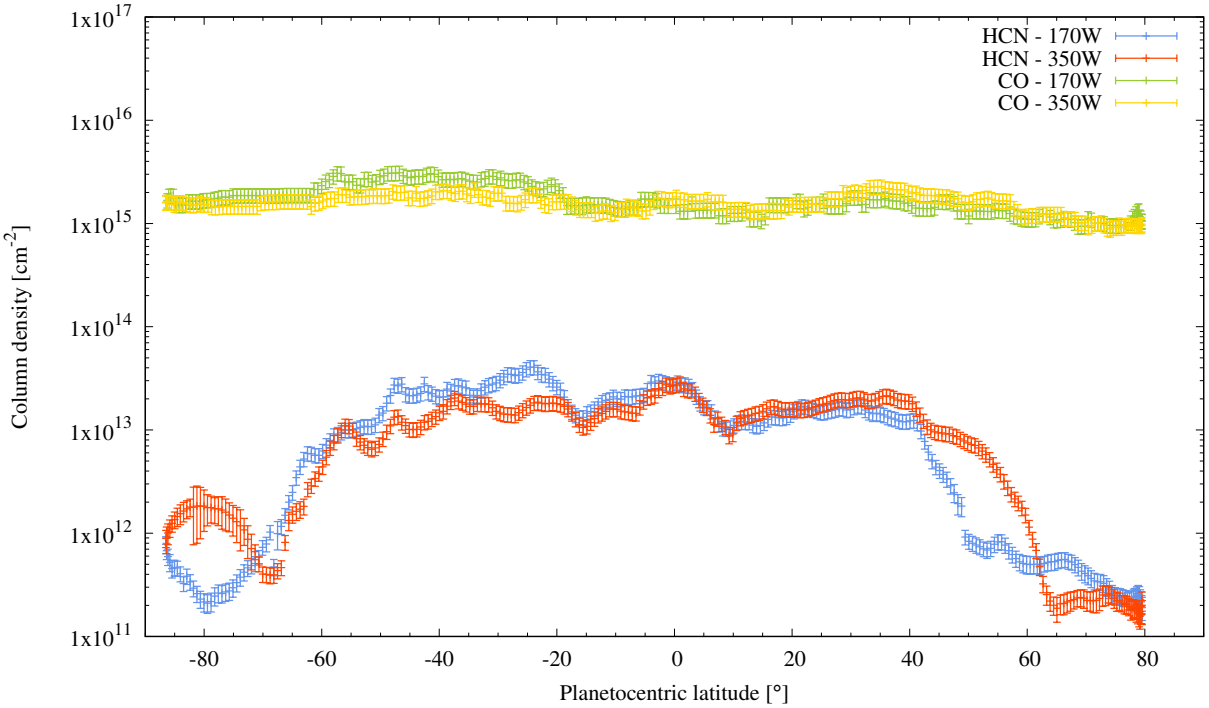

Figure 2 HCN and CO column density in cm^{-2} at the longitudes of the two observed limbs as a function of planetocentric latitude.

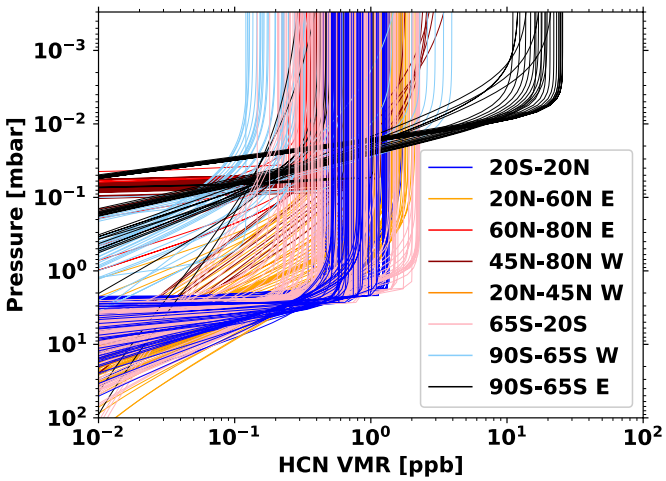

Figure 3 HCN vertical profiles in Jupiter's stratosphere, as retrieved from the ALMA observations of March 2017. They are plotted by latitude bins, except at polar latitudes, where we differentiate profiles seen on each limb: E stands for the eastern limb (350W longitude) and W for the western one (170W longitude).

HCN at polar latitudes

In Figure 4 (left), we compare the column density on the limb with the statistical UV emission of the aurorae at the time of our observations (model of (*24*)), and we find that the HCN depleted region is well correlated with the southern auroral region. Because CO and HCN reside at similar altitude levels in the low-to-mid latitudes, they must be subject to the same circulation regime and

should share the same meridional distribution. The fact that HCN is clearly depleted in the auroral regions between 0.04 and 3 mbar while CO is not can therefore not be caused by a dynamical barrier that would prevent species located in the mid-latitudes to be transported to higher latitudes. Instead, it requires a chemical mechanism specific to HCN. We thus propose that an efficient mechanism at the location of the aurorae of Jupiter must be at play to deplete HCN at pressures of ~0.1 mbar and higher. Energetic electrons are known to precipitate from the magnetosphere down to the upper stratosphere in Jupiter's aurorae and they could destroy HCN. However, we dismiss this possibility because magnetospheric electrons do not penetrate down to mbar pressures in the aurorae (*25, 26*) and therefore they cannot explain the HCN depletion at pressures higher than 0.1 mbar.

A more promising possibility is heterogeneous chemistry with organic aerosols produced in the aurorae. For Titan's atmosphere, *(27)* proposed that the loss to solid haze material is an important sink of nitrogen. This idea was extended by *(28)* and later *(29)*, who showed that introducing a sink term for HCN, representing incorporation into the haze, allowed photochemical model results to better match observations of Titan's HCN and hydrocarbons simultaneously. More recently, *(30)* have demonstrated that HCN bonds efficiently on organic aerosols produced in laboratory experiments under Titan atmospheric conditions when the aerosols reach a given mass and abundance threshold. The conditions under which these experiments were conducted lead to ion-neutral chemistry initiated by a plasma discharge which are comparable to auroral conditions. Besides, enhanced efficiency in C_2 hydrocarbon production has been observed in the aurorae by *(31)*, as initially predicted by models of (*32*). These hydrocarbons are precursors for higher order hydrocarbons. Growing carbon chains eventually lead to the formation of benzene and eventually polycyclic aromatic hydrocarbons (PAHs) in the 10^{-3}–10^{-1} mbar pressure range according to *(33)*. Combining the results of the latter chemistry model with an aerosol microphysical model, *(34)* showed that, among PAHs, pyrene first condenses when the pressure exceeds 0.1 mbar and serves as condensation nuclei for phenanthrene and naphthalene. The resulting particles sediment and continue to grow to form aerosols between 0.1 and 1 mbar. Indeed, abundance peaks of stratospheric aerosols have been found in the middle stratosphere at auroral latitudes (*35*). Our observations now demonstrate that HCN is removed from the gas phase at pressures higher than ~0.1 mbar in the aurorae where models predict large aerosols start to form. The fact that HCN is removed not only under the aurorae, but also in the surrounding longitudes (but still at polar latitudes), probably results from their contamination by aurora-produced aerosols (*35*). Outside the polar region, HCN is no longer depleted between 0.04 and 3 mbar, because there are no more aerosols in the relevant pressure range (*35*).

HCN interior of the southern auroral oval

In Figure 4 (right), a local increase of the column density can be spotted on the eastern limb at the location of the southern aurora. It can be seen in the data shown in red in Figure 2 in the 75°S-85°S range and corresponds to the vertical profiles plotted in black in Figure 3. It reflects an increase in the line emission interior of the southern auroral oval, a region where auroral heating at mbar and sub-mbar levels is known to be significant (*31, 36*). Since our temperature model is inherently limited by the interpolation that we apply in the few gaps in the coverage of the auroral regions the Gemini/TEXES data have, we may be missing the peak in auroral temperatures that could account at least partially for the excess of HCN emission seen interior of the southern oval. However, even increasing the sub-mbar temperatures to 210 K decreases the sub-mbar HCN mole fraction only by ~20%. There is thus a ~10 times higher abundance of HCN at sub-mbar pressures interior of the southern aurora compared to the surrounding polar region. Interestingly, observations and models have demonstrated that HCN can be formed by ion-neutral chemistry

under auroral-like conditions in Titan's N_2-CH_4 atmosphere (e.g., *37, 38*). And *(30)* found evidence that HCN formed under such conditions does not bond on organic aerosols (as discussed previously) until small primary monomers have coagulated into large 100 nm-sized monomers. We propose that HCN is formed similarly in Jupiter's aurorae and that the source of nitrogen is molecular N_2 quenched at kbar pressures from the thermochemical equilibrium between NH_3 and N_2. According to the model results of *(39)*, fitting the observed NH_3 abundance results in an N_2 abundance of ~10^{-5} in the upper troposphere. This N_2 is transported at all latitudes up to its homopause which resides at 0.1-1 µbar. It is only ionized in the aurorae by magnetospheric electrons, which peak in the 10 nbar-0.1 mbar (*25, 26*), to produce HCN. This excess of HCN only produced in the jovian aurorae would not contaminate other regions of the planet and would not perturb the SL9-derived HCN found elsewhere in the atmosphere. Indeed, it would remain confined inside the aurora by the auroral winds observed by *(22)* at least down to pressures where it would be removed by the aerosols. It remains to be shown by chemistry models that this scenario is valid and that HCN can indeed be produced in such amounts in the aurorae (and not elsewhere on the planet) essentially from the dissociation of N_2 coming from the interior by energetic electrons precipitating from the jovian magnetosphere.

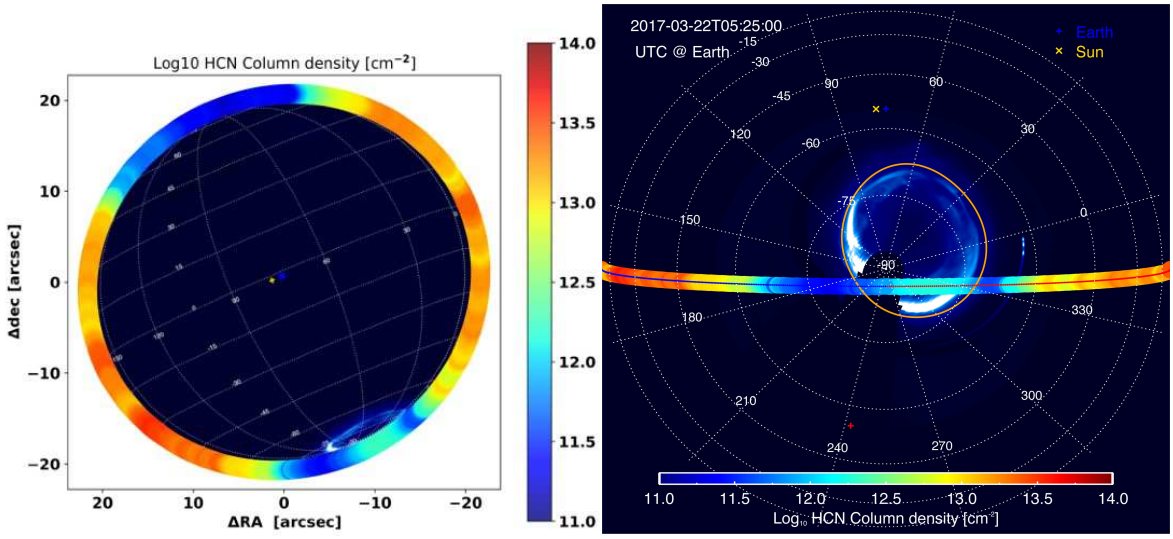

Figure 4 Decimal logarithms of the HCN column density in cm^{-2} represented according to the observation geometry to show the correlation between the HCN depleted region and location of the statistical UV emission of Jupiter's aurorae (24). While the southern aurora is clearly in the field, the northern aurora was rising on the northwest limb and is barely visible on the plot. The left panel shows a global view representative of the observation geometry and the right panel is a polar projection of the southern hemisphere to highlight the variability of the HCN column density over southern polar and auroral regions.

A discrepancy between the HCN and CO_2 horizontal distributions?

SL9-derived species like HCN, CO, H_2O and CO_2 are expected to see their stratospheric abundances evolve both vertically and horizontally following the comet impacts in 1994. However, the ALMA observations of HCN and CO in March 2017 may offer us an explanation for the different meridional distributions seen in HCN and CO_2 with Cassini/CIRS in December 2000.

Apart from the polar regions, the HCN and CO distributions are relatively uniform as a function of latitude. Their vertical profiles share the same cut-off pressure level of 3±1 mbar, derived uniformly for CO and at low-to-mid latitudes for HCN. This level is consistent with the progressive downward diffusion expected for SL9-derived material since the impacts of the comet: 0.2±0.1

mbar in 1994–1995 and $0.3^{+0.2}_{-0.1}$ mbar in 1998 (*9, 13, 15*), and 2±1 mbar in 2010 (*23*). If CO_2 is a daughter molecule of SL9-derived H_2O and CO, then CO_2 should reside at roughly similar levels as H_2O and CO (and thus HCN). This raises two issues. First, this implies that HCN and CO_2 should not be subject to significantly different transport regimes, as hypothesized by *(18)*, to explain the different HCN and CO_2 meridional distributions. Another issue is that it required CO_2 to be located near or below the 5-mbar level in 2000. However, neither H_2O nor HCN and CO had yet reached that level in 2010 and 2017, respectively.

What can then be the cause of the CO_2 peak observed in 2000 at the South Pole? *(18)* investigated the CO_2 distribution with the combination of a transport model and a simplified chemical model. They managed to produce a peak of CO_2 at the South Pole from the conversion of SL9-derived CO and H_2O, complemented by an auroral source of H_2O, in the form of an influx of OH. However, they could not properly fit the CO_2 bulge despite unrealistically high auroral fluxes. They also considered a case, in which CO_2 would not be due to SL9 but solely to auroral precipitation of atomic oxygen. This model was not deemed reasonable, because the asymmetry seen in the CO_2 distribution between the northern and southern polar latitudes, with a peak only seen at southern polar latitudes, implied that northern auroral precipitation be 5 times smaller than in the south.

(21) could not model the disk-averaged decrease in H_2O abundance seen over nearly two decades with Odin and suggested that H_2O was destroyed at a higher rate in the aurorae by ion-neutral chemistry not accounted for in their models. If H_2O is indeed destroyed at a higher rate in this region, it will likely form OH radicals. These radicals, in excess with respect to other latitudes, will react with CO to form CO_2. The amount of CO consumed by this extra production of CO_2 would be barely perceptible in the CO column in 2000. The polar excess of CO_2 observed in 2000 represents a mass of ~6×10^{12} g and would thus require 3.8×10^{12} g of CO to be consumed in the southern aurora between 1994 and 2000, i.e., two orders of magnitude less than the CO mass observed in 1995-1998 and attributed to the delivery by SL9 (*15*). With a H_2O/CO mass ratio of ~0.07, the initial H_2O mass was $3.8 \pm 1.0 \times 10^{13}$ g (*13*). The production of the southern polar CO_2 bulge seen in 2000 would thus require 7±2% of the initial H_2O mass to be converted to CO_2 in 2000, implying thus a more efficient destruction of H_2O than by UV-photolysis and subsequent chemistry alone (*13, 21*). The fact that *(18)* observed a CO_2 peak only over Jupiter's South Pole and not over its North Pole in 2000 would result from the fact that it was the only polar region that had already been contaminated by the SL9-derived material initially deposited at 44°S, as shown in 2D diffusion simulations of *(15)*.

These results shed new light on the coupling between magnetospheres and atmospheres in giant planets. New disk-resolved observations of CO_2 with *JWST* (*40*), possibly coordinated with ALMA mapping observations of CO, HCN, and H_2O, as well as dedicated chemical modeling of Jupiter's auroral regions would certainly help consolidate our findings.

References

1. Spiga et al. 2020. Icarus 335, 113377.
2. Moses et al. 2005. J. Geophys. Res. 110, E08001.
3. Feuchtgruber et al. 1997. Nature 389, 159.
4. Hue et al. 2015. Icarus 257, 163.
5. Hue et al. 2018. Icarus 307, 106.
6. Orton et al. 1995. Science 267, 1277.

7. Moreno et al. 2001. Planet. Space Sci. 49, 473.
8. Sánchez -Lavega et al. 1995. Geophys. Res. Lett. 22, 1761.
9. Lellouch et al. 1995. Nature 373, 592.
10. Marten et al. 1995. Geophys. Res. Lett. 22, 1589.
11. Bjoraker et al. 1996. Icarus 121, 411.
12. Zahnle 1996. In IAU Colloq. 156: The Collision of Comet Shoemaker-Levy 9 and Jupiter, ed. K. S. Noll, H. A. Weaver, & P.D. Feldman, 183-212.
13. Lellouch et al. 2002. Icarus 159, 112.
14. Lellouch et al. 1997. Planet. Space Sci. 45, 1203.
15. Moreno et al. 2003. Planet. Space Sci. 51, 591.
16. Griffith et al. 1997. Icarus 128, 275.
17. Griffith et al. 2004. Icarus 170, 58.
18. Lellouch et al. 2006. Icarus 184, 478.
19. Cavalié et al. 2008a. Planet. Space Sci. 56, 1573.
20. Cavalié et al. 2012. Planet. Space Sci. 61, 3.
21. Benmahi et al. 2020. A&A 641, A140.
22. Cavalié et al. 2021. A&A 647, L8.
23. Cavalié et al. 2013. A&A 553, A21.
24. Clarke et al. 2009. J. Geophys. Res. 114, A05210.
25. Perry et al. 2009. J. Geophys. Res. 104, 16541.
26. Gérard et al. 2014. J. Geophys. Res. 119, 9072.
27. McKay 1996. Planet. Space Sci. 44, 741.
28. Lara et al. 1999. A&A 341, 312.
29. Vinatier et al. 2007. Icarus 188, 120.
30. Perrin et al. 2021. Processes 9, 965.
31. Sinclair et al. 2018. Icarus 300, 305.
32. Wong et al. 2003. Geophys. Res. Lett. 30, 1447.
33. Wong et al. 2000. ApJ 534, L215.
34. Friedson et al. 2002. Icarus 158, 389.
35. Zhang et al. 2013. Icarus 226, 159.
36. Sinclair et al. 2017. Icarus 292, 182.
37. Waite et al. 2007. Science 316, 870.
38. Dobrijevic et al. 2016. Icarus 268, 313.
39. Cavalié et al. 2022. Nature Astronomy, revised.
40. Norwood et al. 2016. PASP 128, 018005.
41. Cavalié et al. 2019. A&A 630, A87.
42. Rohart et al. 1987. J. Chem. Phys. 87, 5794.
43. Dick et al. 2009. J. Quant. Spectr. Rad. Transf. 110, 619.
44. Borysow et al. 1985. ApJ 296, 644.
45. Borysow et al. 1988. ApJ 326, 509.
46. Borysow and Frommhold 1986. ApJ 304, 849.
47. Flasar et al. 2004. Nature 427, 132.
48. Giles et al. 2020. Icarus 350, 113905.
49. Cosentino et al. 2017. J. Geophys. Res. 122, 2719.
50. Twomey 2002. Introduction to the mathematics of inversion in Remote Sensing and Indirect Measurements, 2nd edn. (Dower Phoenix).

Acknowledgments

T.C. acknowledges funding from CNES and the Programme National de Planétologie (PNP) of CNRS/INSU.

This paper makes use of the following ALMA data: ADS/JAO.ALMA\#2016.1.01235.S. ALMA is a partnership of ESO (representing its member states), NSF (USA) and NINS (Japan), together with NRC (Canada), MOST and ASIAA (Taiwan), and KASI (Republic of Korea), in cooperation with the Republic of Chile. The Joint ALMA Observatory is operated by ESO, AUI/NRAO and NAOJ.

Author contributions

T.C. and L. R. performed the modeling and data analysis. All authors discussed the results and commented on the manuscript.

Data availability

Data and material that support the findings of this study are available upon request by contacting the corresponding author.

Code availability

Software used to obtain and process the radar echo time series is available upon request by contacting the corresponding author.

Competing interests

Authors declare that they have no competing interests.

Supplementary Material - Materials and Methods

1. Observations

We use the observations of Jupiter, performed with ALMA on March 22nd, 2017, as part of the 2016.1.01235.S project, which have enabled mapping the winds in Jupiter's stratosphere (*22*). The rather short integration time of 24 minutes limits the longitudinal smearing to 15°. The sub-observer latitude of -3° ensures that only the northernmost latitudes were unobserved.

The planet was mapped with 42 antennas using 39-point mosaic, because of its 43.82" angular size. With the C-1 compact antenna configuration, the resulting elliptical synthetic beam was 1.2" (East-West) x 1" (North-South). Jupiter's disk is thus fully resolved, with a resolution of up to 3° at equatorial latitudes. The spectral setup simultaneously covered the HCN (4-3) and CO (3-2) lines at 354.505 and 345.796 GHz, respectively, with spectral resolutions of 122 and 488 kHz, respectively. Such a high spectral resolution enables fully resolving the lineshape of the HCN and CO lines, which have full widths at half-maximum in the range of 2–10 MHz. It is thus possible to determine the vertical profile of the observed species.

(22) reduced the data using CASA 4.7.2 and applied bandpass, amplitude and phase calibration. The final Jupiter spectral images show HCN and CO emission concentrated at the planet limb. We took the 557 HCN spectra and 540 CO spectra they extracted from the limb (at the 1-bar level) to carry out our analyses. The beam was oversampled by a factor of four to five and the spectra were obtained from a bilinear interpolation of the spatial pixels of the data cube.

2. Spatial distribution retrieval method

We analyzed each CO and HCN limb spectrum with a model that enabled us to retrieve their vertical profile all along the limb. This model is composed of a forward radiative transfer model

and an iterative retrieval algorithm relying on a three-parameter function for vertical profile parametrization. We detail these two components hereafter.

2.1 Forward model

2.1.1 Radiative transfer

We used the radiative transfer model described in *(41)* adapted to Jupiter's atmosphere. It accounts for the 3D ellipsoidal geometry of the planet. We take the ephemeris from JPL Horizons Solar System Dynamics ephemerides (https://ssd.jpl.nasa.gov/horizons/) to have the planet geometrical data at the time of the observations. In particular, we use the equatorial angular diameter, the observer sub-latitude and sub-longitude, North Pole angle, and geocentric distance.

The spectroscopic data for both lines come from the JPL catalog. We adopted a pressure broadening coefficient γ of 0.145 $cm^{-1}.atm^{-1}$ and a temperature dependence exponent n of 0.75 for the HCN line according to *(42)*. For the CO line, we took $\gamma = 0.067$ $cm^{-1}.atm^{-1}$ and n=0.60, according to *(43)*.

The continuum is formed from the collision-induced absorption of H_2–He–CH_4 (*44-46*) and the far wings of NH_3 and PH_3 lines. We parametrize the vertical profile of both species using $q = q_0 \left(\frac{p}{p_0}\right)^{(1-f)/f}$ with deep mole fractions q_0 of $2x10^{-4}$ and $6x10^{-7}$, cut-off pressures p_0 of 800 and 500 mbar, and fractional scale heights f of 0.15 and 0.2, for NH_3 and for PH_3, respectively.

2.1.2 Temperature field

The temperature vertical profile in the stratosphere of Jupiter shows meridional, and (to a smaller extent) zonal variability over the course of only a few weeks in several regions like the equatorial and auroral regions (e.g., *47, 48*). Fortunately, Jupiter's stratospheric temperatures were mapped with Gemini/TEXES a few days apart from our observations. The temperatures of the equatorial zone up to the mid-latitudes were measured on March 14, 16 and 20, 2017 by *(49)*. The polar region temperatures were retrieved by Sinclair et al. (in preparation) from observations recorded on March 17–19, 2017.We reconstructed a full 3D temperature field from these combined data, and filled the latitudinal and longitudinal gaps by interpolating linearly between the data points. To speed up the retrievals, we used 2D latitude/pressure maps instead of the full 3D temperature field. We extracted these 2D thermal maps from the 3D field at 350W (eastern limb) and 170W (western limb). They are displayed in Figure 5 and account for the 15° longitudinal smearing of the observations. Note that the heating caused by the northern and southern auroras can be seen on the 170W and 350W plots, respectively. In a first and simple approach, we do not consider the temperatures at other longitudes in our radiative transfer calculations and essentially work with 2D fields (pressure-latitude) for each limb.

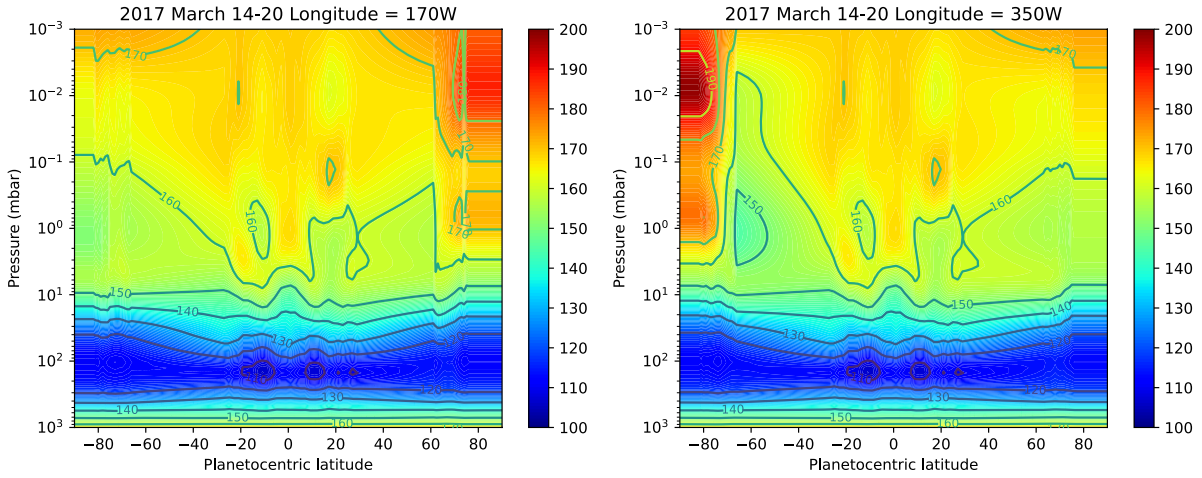

Figure 5 Temperature field at 170W (left) and 350W (right), which correspond to the eastern and western limbs, respectively, as measured with Gemini/TEXES on March 14–20, 2017.

2.2 Retrieval model

With known temperature and pressure fields, we used the ALMA observations to obtain vertical profiles of volume mixing ratio of HCN and CO. The mixing ratio as a function of height in km above the 1 bar level, f(z), is parameterized with three independent numbers, a_1, a_2, a_3 as follows:

$$f(z) = a_1[1 + \tanh(z - a_2)/a_3]$$

The inverse problem is then to find only three numbers at each of the limb spectra, where a_1 is the high altitude asymptotical constant mixing ratio above a transition level, a_2 is the altitude of this transition level, and a_3 is a scale height informing how quickly the mixing ratio decreases below the transition level with decreasing altitude.

The choice of this parametrization provides several advantages worth pointing out. With only three unknown the inverse problem is robust and stable, it is relatively fast, and it does yield already a high quality of fitting (see Figure 6), indicating that we exploit most of the information content of the spectra. In addition, the parameterized vertical profiles capture the key physical behavior of the actual HCN and CO mixing ratios with cut-off height as a free parameter.

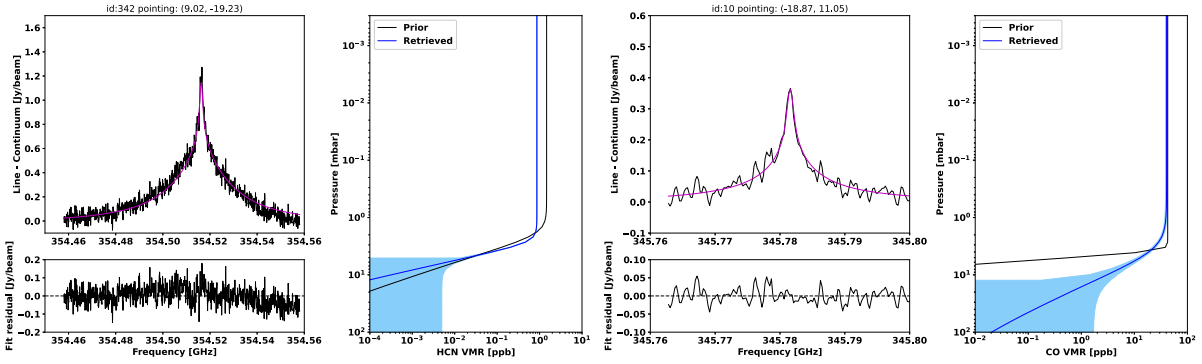

Figure 6 HCN (left) and CO (right) volume mixing ratio (VMR) vertical profile retrieval examples (blue curves) with shaded region encompassing the range of 1-σ uncertainties due to random measurement errors, and (black) the starting profile. The measurement spectra (black) and fitted spectra (magenta) along with the residuals are shown as well.

We solved the inverse problem with an iterative damped least-squares method, also known as Twomey–Tikhonov in Earth atmospheric science literature (*50*). The three parameters are assembled into a vector $\boldsymbol{x}$, and the next iteration is obtained as

$$\boldsymbol{x_{i+1}} = \boldsymbol{x_i} + (\boldsymbol{K^T S_e^{-1} K} + \boldsymbol{R})^{-1}[\boldsymbol{K^T S_e^{-1}} \mathbf{\Delta y} - \mathbf{R}\boldsymbol{x_i}].$$

The Jacobian matrix $K = \frac{\partial y_n}{\partial x_m}$, where y_n is the n-th spectral channel of the forward model, was estimated numerically perturbing each of the three parameters by a small amount and recalculating forward model spectra. This matrix remains constant during iterations. The diagonal matrices $\boldsymbol{S_e}$ and $\boldsymbol{R} = \alpha \boldsymbol{I}$ denote random measurement noise (1-σ) and a regularization operator respectively. The regularization parameter, α, was estimated by trial and error with synthetic inversions and then fixed for all subsequent iterations of all retrievals. The $\boldsymbol{\Delta y}$ term holds differences between measured and calculated spectra for the current estimate of $\boldsymbol{x}$. The iterative process continues while the current reduced χ_i^2 is smaller than the one from previous iteration within a threshold of 0.5%.

The retrieval process described above requires an initial estimate on the three parameter values for each new observation. For the first inverted spectrum, these were supplied manually based on few trials. For subsequent points on the map, they were however taken from the previously inverted measurement before running the first retrieval iteration. This approach is reasonable as we expect adjacent points on the map not to deviate strongly one from another (in mixing ratio). For validation of our assumption, we investigated the spectral line characteristics of adjacent observations. Finally, the least-squares method allowed us to estimate how the random error component in the measurements gets projected into uncertainties in retrieved parameters through the solution covariance matrix. The diagonal elements were used in plotting the retrieved profile uncertainties (as shaded regions in Figure 6) which are generally smaller than 3% on the a_1 parameter, smaller than 1% on the a_2 parameter, and in the 5-10% range on the a_3 parameter.

Random samples of retrieved HCN and CO profiles with the corresponding spectra and fit are displayed in Figure 6. About 95% of HCN retrievals converge automatically to the set criteria, and about 98% in case of CO which is more optically thin. In the few cases which did not automatically converge, we supplied manually a better initial value of the a_2 parameter which allowed the inverse problem to proceed nominally to convergence.

In addition, we investigated the role of the full 3D temperature field on the mixing ratio retrievals, especially at auroral latitudes where sharp gradients may exist. We compared forward radiative calculations using the retrieved volume mixing ratios and the full 3D temperature field, with calculations using the same abundance profiles and the 2D temperature maps produced for the two limbs (Figure 5). In the majority of cases, the 3D temperatures did not play any role. However, in a few cases, we identified a need to consider the full 3D inputs in the inversion of the HCN profiles. In these limited cases where the 2D temperatures would produce a fit outside the measurement noise, we rerun the retrieval procedure with the full 3D temperature field. These cases represent less than 5% of the HCN spectra and are located at 33°S–46°S and 53°S–57°S on the eastern limb and 64°S–69°S on the western limb.